



# Multi-resolution dictionary learning for discrimination of hidden features: A case study of atmospheric gravity waves

Varanasi Satya Sreekanth<sup>a,b,\*</sup>, Karnam Raghunath<sup>a</sup>, Deepak Mishra<sup>b</sup>

<sup>a</sup> National Atmospheric Research Laboratory, Department of Space, Gadanki, Pakala, 517112, Andhra Pradesh, India

<sup>b</sup> Indian Institute of Space Science and Technology, Department of Space, Valiyamala, Thiruvananthapuram, 695547, Kerala, India

## ARTICLE INFO

### Article history:

Received 29 October 2021

Revised 11 October 2022

Accepted 30 October 2022

Available online 1 November 2022

### Keywords:

Dictionary learning

Multi-resolution

Sparsity

Doppler shift

Lidar

Gravity waves

## ABSTRACT

In this work, we propose Multi-Resolution Dictionary Learning by promoting sparsity, and Instantaneous Frequency Estimation technique for the discrimination of measured parameter from the effect of unknown sources like noise, and natural phenomena that occur in background during the data acquisition. The Dictionary Learning technique using Multi-Resolution Analysis is performed in the Wavelet Analysis domain using Singular Value Decomposition. In this paper, we aim for the discrimination of contribution from unknown sources in the measured parameter in the amplitude domain and frequency domain by promoting sparsity and Instantaneous Frequency Estimation respectively. We implement the proposed technique and discuss its potential with a case study on the discriminating the Doppler shift in Atmospheric Gravity Waves that occur due to the horizontal wind during data acquisition.

© 2022 Elsevier B.V. All rights reserved.

## 1. Introduction

The representation of measured parameter profiles( $\mathbf{Y}$ ) in the Dictionary Learning setting in the matrix form as the linear combination of a product of Dictionary matrix( $\mathbf{D}_{\text{eff}}$ ) and sparse matrix  $\mathbf{X}$ , with noise( $\mathbf{V}'$ ) is given in (1), where the Dictionary matrix provides the spatial information, and the sparse matrix provides the temporal information. Initially, the Sparse matrix( $\mathbf{X}$ ) is initialized with zeros as its elements. Both  $\mathbf{D}_{\text{eff}}$  and  $\mathbf{X}$  are updated during the update phase of the Dictionary Learning. In this work, the lower case bold letters and lower case letters represent the column vectors of the matrix and elements of the corresponding matrix respectively.

$$\mathbf{Y} = \mathbf{D}_{\text{eff}}\mathbf{X} + \mathbf{V}' \quad (1)$$

where  $\mathbf{Y} \in \mathbb{R}^{n' \times m'}$ ,  $\mathbf{D}_{\text{eff}} \in \mathbb{R}^{n' \times K'}$ ,  $\mathbf{X} \in \mathbb{R}^{K' \times m'}$ ,  $\mathbf{V}' \in \mathbb{R}^{n' \times m'}$ ,  $n'$ , represents the number of range bins(spatial information),  $m'$  is the number of profile integration's(temporal information), and  $K'$  is an arbitrary size.

### 1.1. Related work

There exists several Multi-Resolution retrieval techniques like filtering, Steerable pyramid, Multi-Resolution Analysis(MRA) [1–3],

and Wavelet Packet Decomposition(WPD). Applications of steerable pyramids are seen in image processing. The MRA is an application of filter-bank techniques associated with orthogonal wavelets. The measured parameter profiles are decomposed into detail coefficients and coefficients with different resolutions. It was reported in [4] that time-frequency feature extraction for each resolution, improves the separability of the contribution of the unknown sources in the measured data. Although the fixed basis techniques like Discrete Fourier Transform(DFT), Discrete Cosine Transform(DCT), and Discrete Wavelet Transform(DWT), require feature extraction techniques to get sensitive information. The techniques for the Dictionary initialization, Dictionary update, and sparse coding algorithms are given in [5–7]. A detailed survey on sparse representations using  $l_1 - l_2$  norm in the Dictionary Learning setting is reported in [8]. Techniques for combining the fixed basis and adaptively learned Dictionaries are reported in [9]. A Multi-scale Dictionary Learning algorithm using Wavelets is reported in [10] with application to image processing by decomposing the image to different scales and learning the Dictionaries for each scale for having the effective representations.

The idea of combining MRA with WPD is reported in [10], and is applicable to discriminate the measured profiles from the effect of background sources. The multi-resolution decomposition based on WPD when combined with Dictionary Learning have the lowest Reconstruction Error(RE) compared to other multi-resolution representations, and considered for the present work.

\* Corresponding author.

E-mail address: [sreekanth@narl.gov.in](mailto:sreekanth@narl.gov.in) (V.S. Sreekanth).

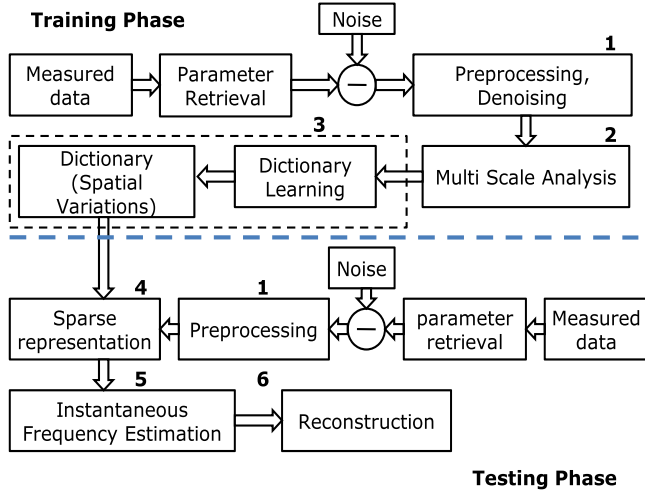


**Fig. 1.** Workflow diagram for analysis of effect of background sources in the parameter profiles. Intermediate stages include preprocessing, training, testing, multi-resolution representations, Dictionary Learning, Instantaneous Frequency Estimation, and reconstruction. The numbers on each block represent the block numbers and are used for only better understanding of the technique.

### 1.2. In this paper

In the Sparse Coding Stage of Dictionary Learning technique, we employ the Sparsity promotion by  $l_2/l_0$ -norm for removing the contribution of background sources in the measured data in the amplitude domain and in the frequency domain through Instantaneous Frequency Estimation(IFE) [11]. In this paper we construct multi-resolution dictionaries and apply them, to specific case study of discrimination of Doppler shift in Gravity Waves due to background horizontal wind.

### 1.3. Paper organization

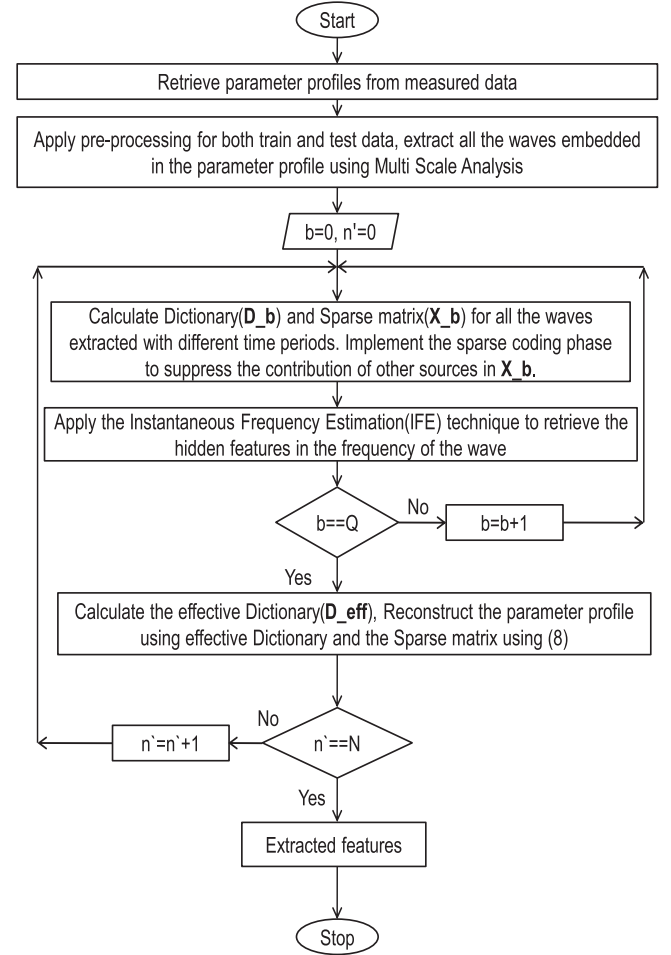
Introduction to the research problem, related research works, Multi Resolution Analysis is explained in Section 1. Section 2 is on the methodology of MRDL by promoting sparsity for reducing the effect of background sources on measured parameter profiles. Section 3 describes the application of the proposed methodology for reducing the effect of background wind in the temperature perturbations by Dictionary Learning through Sparsity. A detailed application procedure for interpretation of Lidar observations through MRDL using the wavelets, and IFE for removing the effect of horizontal background wind in temperature perturbation is discussed. A detailed analysis on the distribution of Doppler shift and its seasonal variations are discussed. Section 4 is about Conclusion on the performance of the proposed method.

## 2. Multi-resolution dictionary learning

The block diagram and the flowchart for reducing the effect of background sources in the measured parameter profiles in amplitude domain and frequency domain are given in Figs. 1 and 2 respectively. The Dictionaries are learned from the training data perturbations to optimally represent test data using Sparse coding. In the present work, the term 'Multi-Resolution' refers to temporal variations.

### 2.1. Selection of parameters

The regularization parameter( $\alpha$ ) [12] turns the algorithm to more generalized model by promoting the sparsity. In the learn-



Q= Number of Levels of Decomposition

**Fig. 2.** Flowchart for the retrieval of the hidden characteristics in the parameter profiles.

ing problems, specifically when measurements taken in noisy conditions, the learning model suffers the problem of overfitting resulting in the poor performance of the model. To avoid this, a constraint is added to the optimization problem. In the present work, the regularization parameter is equal to 1. The error tolerance represents the maximum allowable difference between the true value and the reconstructed value. Another important parameter that affects the computations in the learning process is the 'Patch Size' [13]. Selection of proper patch size reduces the computational time required while implementing the algorithm and also retain local features of the data. The number of iterations is dependent on the convergence of the algorithm.

Fixed Basis are the predefined Dictionaries such as wavelets, and transform techniques. Fixed transforms are not data adaptive and have redundancy in the tasks like denoising, feature extraction, and classification. Using wavelets [1], we can decompose the data into multi-resolutions that makes us to choose wavelets as fixed basis. To exploit the redundancy retained by wavelet decomposition, we are implementing the Multi-Resolution Dictionary Learning in the Wavelet analysis domain.

### 2.2. Learning in wavelet domain

We train and update the Dictionary using the procedure reported in [6]. The wavelet domain Dictionary Learning is the same

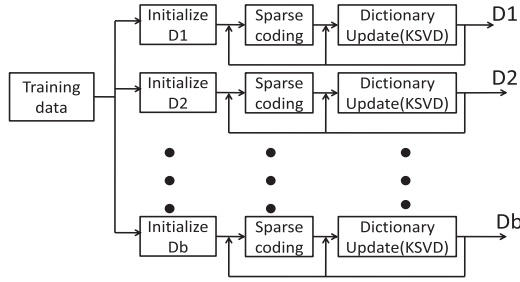


**Fig. 3.** Methodology for Multi-Resolution Dictionary Learning. Sparse coding and Dictionary update using K-Singular Value Decomposition is implemented for all the profiles with different resolutions individually.  $D_1, D_2 \dots D_b$  denote the Dictionaries learned corresponding at each resolution using MRA.

as the training the data in the analysis domain( $\mathbf{W}_A$ ) of multi-resolution representations. Figure 3 is the internal representation of Multi-Resolution Approximation and Dictionary Learning of Fig. 1.

For the each level of wavelet decomposition that represent temporal variations of measured data profile with specific resolution, separate Dictionaries and sparse matrices are learned in the wavelet analysis domain and the mathematical representation of the complete process is given in (4).

$$\forall b \arg \min_{D_b, X_b} \|(\mathbf{W}_A \mathbf{Y})_b - D_b X_b\|_F^2 \text{ s.t. } \|x_{i,b}\|_0 \leq \epsilon \quad (2)$$

where  $\epsilon$  represent the error tolerance( $=10^{-2}$ ). The detailed sequence of steps for the implementation of Multi-Resolution Dictionary Learning is given in Algorithm 1. The Dictionary( $D_b$ ) at each

**Algorithm 1** Multi-Resolution Dictionary Learning(MScDL).

**Input:** tolerance( $\epsilon$ ), regularization parameter( $\alpha$ ), patch size, training data, test data, no. of. iterations, type of wavelet, no. of. decomposition levels, no. of. atoms, size of dictionary

**Output:** The  $D_b$  combined with DWT, give the effective multi-resolution Dictionary( $D_{\text{eff}}$ ).

**if** (SNR > 3) & (observation time  $\geq 4$  h) **then**

- for b in range(1,Q,1):
  1. set  $D_b = 0$ .
  2. Learn and update the  $D_b$  separately for all decomposition using KSVD.
  3. Solve (4) for sparse representation( $x_b$ ) of each resolution using the iterative shrinkage Algorithm.
- Compute  $D_{\text{eff}}$ , where  $D_{\text{eff}}$  is the union of all Dictionaries learned at each level of decomposition using step 2.

**else**

**end**

Look for other data.

**end**

resolution is a product of fixed basis(B) and adaptively learned dictionary( $D$ )

$$(D_b)_{n' \times K'} = B_{n' \times K'} (D)_{n' \times K'} \quad (3)$$

where  $1 \leq b \leq Q$ ,  $Q$  represent the total number of levels of decomposition obtained after applying MRA to the temperature perturbations. The fixed basis is a kernel function.

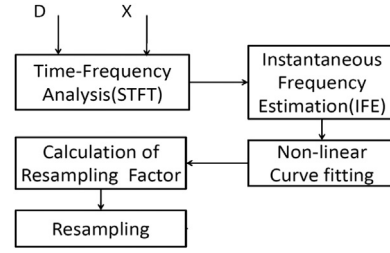


**Fig. 4.** Methodology for the calculation of the resampling factor. The resampling factor is calculated from the rows of sparse matrix, that gives the temporal information.

### 2.3. Sparse coding

The optimization problem for sparse coding in the analysis domain is expressed in (4).

$$\min_x \|x\|_{2,0}^0 \text{ subject to } \|\mathbf{W}_A \mathbf{y} - D\mathbf{x}\|_2 \leq \epsilon \quad (4)$$

Eq. (4) is solved using iterative shrinkage algorithm reported in [14].

The sparse coding recovery problem is usually formulated by the following  $l_2/l_0$  norm minimization problem (5) where  $\epsilon$  limits the  $l_2$ -norm for the noise in the measurements.  $\|x\|_{2,0}$  stands for  $l_2/l_0$  norm of  $x$ ,

$$\|x\|_{2,0} = \|\beta\|_0 \quad (5)$$

where  $\beta = [\|b'_1\|_2, \|b'_2\|_2, \dots, \|b'_{n'}\|_2]^T$ ,  $b'_1, b'_2 \dots b'_{n'}$  are columns of  $x$ . The  $\|x\|_{2,0}$  is equivalent to the sparse matrix.

### 2.4. Optimal dictionary criteria

It is necessary to ensure that the selection of training data is a combination of all variations. After learning the Dictionary using training data, the Dictionary is quantified as the optimal based on Mutual Coherence( $\mu$ ). If the atoms of the Dictionary matrix are highly correlated, the value of  $\mu = 0$  and it will be difficult to distinguish the effect of background sources on measured data profiles. A lower value of  $\mu$  guarantees that the learned Dictionary is suitable for optimal data representation. The techniques for learning Dictionaries with self-bounded coherence is explained by Sigg et al. [15].

### 2.5. Instantaneous frequency estimation

The methodology for removing the effect of background sources is dependent on calculating the resampling factor(n) using Instantaneous Frequency Estimation(IFE) technique reported in [11,16]. Fig. 4 is the internal representation of Instantaneous Frequency Estimation of Fig. 1. The Instantaneous Frequency(IF) vector is the frequency plane projection of the time-frequency distribution. The determination of the resampling factor(n) is obtained by non-linear curve fitting and is the core work to be carried out. The frequency at each decomposition level is resampled by using the resampling factor, and the difference between the original frequency of the data and resampled frequency give the change in frequency due to the background sources in frequency domain and is the resultant of the IFE technique.

The effect in frequency domain is reduced by the resampling sequences in time domain with the resampling factor obtained after the curve fitting.

$$n = \frac{f'_1}{f_1} = \frac{f'_2}{f_2} = \frac{f'_3}{f_3} = \dots = \frac{f'_{n'}}{f_{n'}} = \frac{f_s}{f_0} = \text{constant} \quad (6)$$

**Table 1**  
Input and output.

Block Name (Block number)	Input	Output
Parameter data (1)	Temporal Variations	Preprocessed data
MRA(2)	Temporally varying data	Temporal profiles decomposed to 5 levels
Dictionary Learning, Dictionary(3)	Each individual level of all temporal profiles	Dictionary Matrix ( $D_b$ ), Sparse matrix(X) Sparse matrix ( $X_b$ )
Sparse Representation(4)	$(D_b)_i, (X_b)_i \forall 1 \leq b \leq Q; 1 \leq i \leq n'$	$X_b$ after applying $l_2/l_0 - norm$
IFE(5)	$X_b$	IF vector, resampling factor
Reconstruction(6)	$(D_b)_i, (X_b)_i \forall 1 \leq b \leq Q; 1 \leq i \leq n'$	$D_{eff}, X_{eff}$ , and $\hat{Y}$

where  $f_1, f_2, \dots, f_N$ , and  $f'_1, f'_2, \dots, f'_{n'}$  denote the Instantaneous Frequencies of the signal with Doppler shift, and signal after compensating with the Doppler shift respectively.  $f_s, f_0$  denote the sampling rate and the IF of the original signal. The resampling interval of the signal acquired is determined by using (6) and (7).

$$\Delta t_i = \frac{f_0 \times \Delta t}{f_i} \quad (7)$$

where  $\Delta t_i$  and  $\Delta t$  denote the sampling interval of the signal without the effect of the background source and the measured data, respectively.

### 2.6. Reconstruction of profiles

For having a combined reconstruction of the measured data profile, two operations are required to be computed, the first is multiplication by the complete equivalent Dictionary( $D_{eff}$ ) achieved by multiplying each explicit sub-dictionary( $D_b$ ) by the appropriate sparse matrix( $x_b$ ). The effective reconstruction of the measured profile( $y$ ) in analysis domain for all the resolutions is expressed in mathematical form as (8).

$$\hat{Y} = W_s D_{eff} X = W_s \left( \bigcup_b \bigcup_{k'} D_b \hat{x}_b^{k'} \right) \quad (8)$$

where  $W_s$  represent the transformation in the synthesis domain,  $\bigcup_b D_b, \bigcup_{k'} \hat{x}_b^{k'}$  give temporal information, and spatial information. The input and output at each block in Fig. 1 are given in Table 1.

## 3. Discussions and results: application to atmospheric gravity waves

The output of the Rayleigh Lidar system is the spatial and temporal collection of photon count profiles, and the temperature profiles are retrieved using the algorithm reported in [17]. Perturbations in the middle atmosphere temperatures are observed over vertical heights varying from few meters to kilometers are believed to be due to the superposition of GWs. Lidar is still the only technology that allow to measure temperature( $T$ ) with sufficiently Spatial and temporal resolution in the stratosphere and in the Mesosphere heights. The GW induced temperature perturbations( $T'$ ) [18] are obtained by decomposing the measured temperatures profiles( $T$ ) into local background( $T_0$ ) and perturbations around this background are calculated by using (9).

$$T'(z, t) = T(z, t) - T_0(z, t) \quad (9)$$

All the parameters  $T, T_0$ , and  $T'$  are dependent variables of the altitude( $z$ ) of the atmosphere and the time instant( $t$ ).

### 3.1. Introduction to the problem

Before analyzing for the signatures of Gravity Waves(GW) from temperature perturbations, it is essential to remove the effect of atmospheric background sources such as horizontal background wind, and planetary wave sources that trigger instabilities. These instabilities are sometimes misinterpreted as Gravity waves. For

the present work, the data used is acquired using the Rayleigh Lidar system [19] available at National Atmospheric Research Laboratory(13.45°N, 79.17°E), India.

In this work, the presence of horizontal background wind [20] in the measured data profile during acquisition results in the frequency shift (Doppler shift) of the true frequency( $f_{obs}$ ) of the Gravity Wave and is reduced with Multi-Resolution Dictionary Learning by promoting sparsity in the amplitude domain, and by IFE technique in the frequency domain. The retrieved Doppler shift profiles are compared with Doppler shift profiles calculated using(A. 3) from wind velocity profiles obtained using GPS Radiosonde(insitu) [21] and Meteor Radar [22].

The effect of background horizontal wind on Gravity Wave parameters is reported in [20,23]. The background wind in the temperature perturbations lead to an increase in horizontal energy density, and a reduction in vertical energy density at lower and higher frequencies respectively, and above the Buoyancy frequency a high value of Vertical energy density is observed. So before starting for the analysis of AGW, it is essential, first to remove the effect of background sources. The methodologies for the extraction of Gravity Wave parameters are explained in [18,24]. The resultant of the Fast-Fourier Transform(FFT) when applied to spatial and temporal temperature perturbations determine the vertical wavenumber and the time period of the GW respectively.

The Table 2 represent the analogy between the Dictionary Learning and Instantaneous Frequency Estimation to the case study of reducing the effect of horizontal background wind in Atmospheric Gravity Waves.

### 3.2. Selection of data sets and processing

The test data used for the removal of background wind is collected on 21 April 2014, at 20:00 Hrs, Indian Standard Time(IST). The data used for the testing and training phases is largely based on duration of the data acquisition and Signal to Noise Ratio(SNR). In the present work we have considered the data acquisition time longer than 4 h and SNR > 3 based on our previous experience about Gravity Waves. The formula used for the calculation of SNR for the present work is given by (10).

$$SNR = \frac{S}{\sqrt{S + S_{Noise}}} \quad (10)$$

where  $S$  represent the back-scattered photon counts and  $S_{Noise}$  represent the back-scattered photon count due background light. The noise is the mean of all photon counts in the altitude between 150 km and 300 km.

The raw photon count profiles are collected by using the Rayleigh Lidar with temporal and spatial resolutions of 4 min and 300 m respectively. Maintaining acceptable SNR, while keeping resolution as high as possible is the reason for selecting the mentioned specifications. The maximum and minimum vertical wavelength that can be measured is limited by the altitude and system noise respectively. The lower value of an observed period of GWs is limited by integration time associated with individual profiles.



**Table 2**  
Analogy of Dictionary Learning and IFE to the case study of Atmospheric Gravity Waves.

DL and IFE	Gravity Waves	Significance
Measured data ( $\mathbf{Y}$ )	Temperature	Temperature perturbations
Dictionary ( $\mathbf{D}_{\text{eff}}$ )	Altitude profiles	Wavenumber( $k_m$ )
Sparse matrix ( $\bigcup_k \mathbf{x}_b^k$ )	Temporal Information	Frequency of GW ( $f_{\text{obs}}$ )
Noise( $\mathbf{V}$ )	Background noise	Background Light
Reconstructed data( $\hat{\mathbf{Y}}$ )	Temperature profile	Horizontal Wind Free Temperature perturbations
Sampling Rate( $f_s$ )	Temporal Resolution	4.16 mHz (4 min)
IF( $f_0$ )	Temporal Derivative	Altitude Dependent

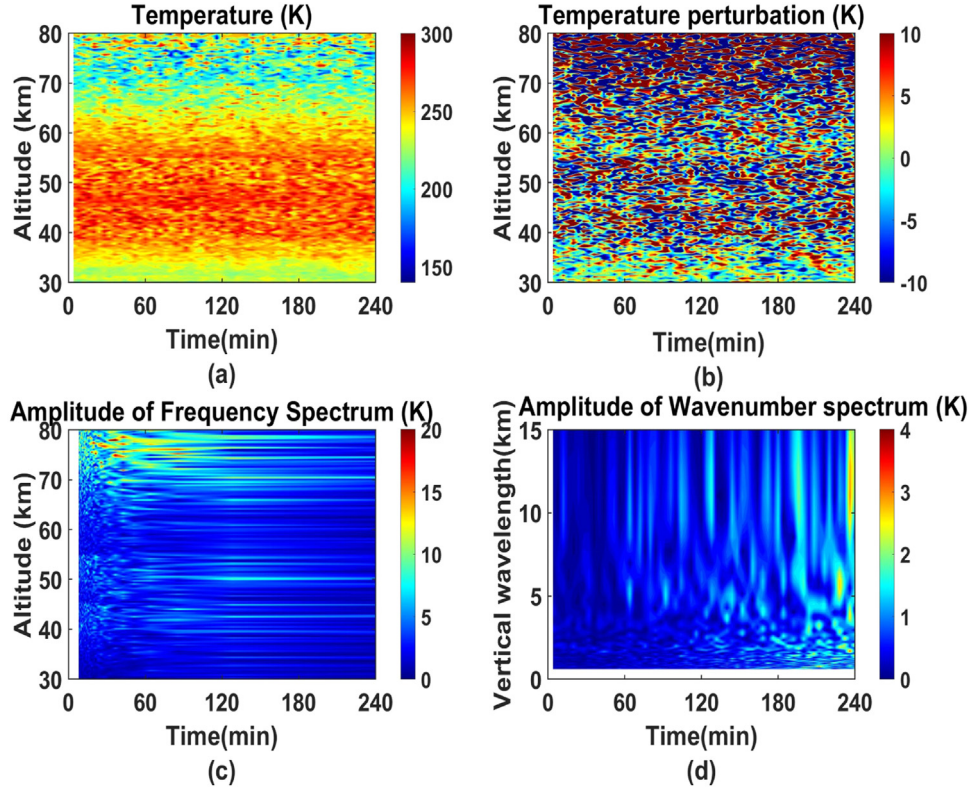


**Fig. 5.** (a). Temperature profiles of test data collected on 21st, April 2014, (b) Temperature perturbations of test data, (c) Frequency domain representation of temporal profiles. The dominant time period of waves is between 15 min to 80 min, (d) Identification of the dominant vertical wavenumber.

The perturbed temperature profile data used for training the Dictionary is collected during the year 2014 using the Rayleigh Lidar at NARL, and the Dictionary is trained with this data for accounting the seasonal changes. The learned Dictionary is then effectively used for sparse representation of the test data.

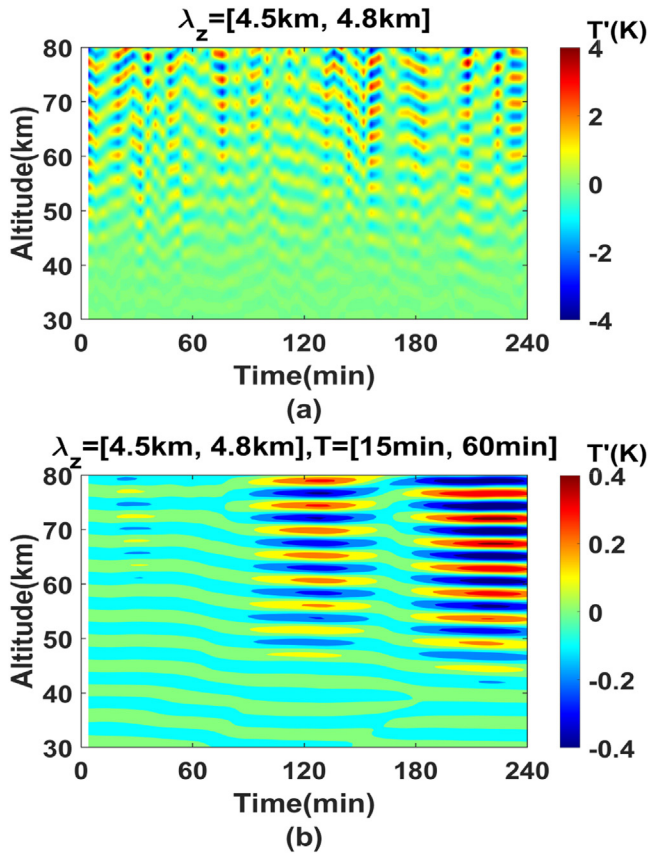
The training data is of size  $184 \times 3046$ . The number of rows in training data and test data represent the spatial resolution, and the columns represent the temporal resolution. The testing data is of size  $184 \times 60$ . The learned Dictionaries and sparse matrices of all the waves are of size  $184 \times 3046$  and  $3046 \times 60$  respectively. The regularization parameter is of value 1, error tolerance( $\epsilon$ ) is 0.01 and the Dictionary update and sparse coding phases are implemented for 80 iterations.

Fig. 5 represents the process of identifying the dominant vertical wavelengths. The Fig. 5(a) Temperature profiles observed for 4 h with temporal resolution of 4 min. The Fig. 5(b) and (c) represent the temperature perturbations and frequency spectrum varying with altitude. From Fig. 5(c) it is observed that the waves with time period of 15 min to 80 min are dominant in the temperature perturbations. Gravity Waves with vertical wavelengths between 4.2 km to 7 km and 9 km to 15 km are dominant in the present data. The dominant vertical number varies between  $2 \text{ km}^{-1}$  and  $4 \text{ km}^{-1}$ , and dominant vertical wavelength between

5 km to 7 km and 9 km to 13 km as observed from Fig. 5(d). The intrinsic frequency and the horizontal wavelength are calculated by using the method proposed in [25] from temperature profiles after background wind compensation.

The bandpass filtering technique is applied to the spatial and the temporal domain of temperature perturbation for having only waves of dominant vertical wavelength and time period. The reason for choosing the dominant waves is that they are the major contributors to the Doppler Shift. The bandpass filtering is applied with a lower cut-off wavelength( $\lambda_{z_L}$ ) and a higher cut-off wavelength( $\lambda_{z_H}$ ) of 4.5 km and 4.8 km respectively. The resultant perturbation profile is seen in Fig. 6(a). Fig. 6(b) represents both spatially and temporally filtered temperature perturbations with a time period 15 min as lower limit and 60 min as the upper limit. The width of temperature perturbation variation (represent Crest and Trough of the Gravity Wave) along altitude is equal to one vertical wavelength cycle as seen from Fig. 6(a).

After identifying the dominant vertical wavenumbers, the temperature perturbations are subjected multi-resolution technique. For each resolution, the Dictionary and Sparse matrices are learned separately from the training set of temperature perturbations. The contribution of horizontal background wind to the energy enhancement of Gravity Waves is corrected by applying the  $l_2/l_0$



**Fig. 6.** (a) Temperature perturbations with vertical wavelength( $\lambda_z$ ) between 4.5 km to 4.8 km. (b) Temperature perturbations with  $\lambda_z$  between 4.5 km to 4.8 km and time period between 15 min to 60 min for the test data collected on 21 April, 2014.

norm for all the levels of decomposition in the sparse coding phase and the contribution of background wind to the frequency is corrected by applying the IFE method.

### 3.3. Performance indicators

To test the proposed method, the Minimum Mean Square Error(MMSE), Peak Error(PE), and Reconstruction Error(RE) are used as the performance indicators. The Eqs. (11), (12), and (13) are used for the calculation of MMSE, PE, and RE respectively.

$$MMSE = \frac{1}{J} \sum_{l=1}^J [\mathbf{y} - \hat{\mathbf{y}}]^2 \quad (11)$$

$$PE = \max_{j=1}^J [\mathbf{y} - \hat{\mathbf{y}}] \quad (12)$$

$$RE = \|\mathbf{y} - \mathbf{D}_{\text{eff}} \mathbf{x}_j\|_2^2 \quad (13)$$

where  $\mathbf{y}$  is the actual measured profile,  $\hat{\mathbf{y}}$  is the reconstructed profile of measured profile,  $\mathbf{x}_j$  denotes the largest number or percentage of  $J$  coefficients in transform domain. The faster the reconstruction error decays, the better the sparse representation.

The proposed method is tested with Wavelet test signals like Doppler, Blocks, Bumps, Heavysine, and Chirp signal to identify the applicability of the proposed method. The Minimum Mean Square Error(MMSE) and Peak Error(PE) are used as performance metrics for the proposed method. The Doppler test signal is used to check the performance of proposed algorithm to the amplitude and the frequency changes, block signals are used to test the algorithm

**Table 3**

Comparison of performance with wavelet test signals.

Test Signal	Doppler	Blocks	Bumps	Heavysine	Chirp
MMSE	1.49e-2	8.32e-5	3.4e-6	1.06e-2	8.744e-12
PE	3.9	0.00981	8.501e-3	1.17	9.18e-5

**Table 4**

Comparison of Performance Indicators as a function of type of Wavelet and the number of levels of Decomposition(Q).

Q	Wavelet	db4	Haar	sym4	coif4	fk4
1	RE	2.487e-12	2.487e-12	4.381e-13	4.377	9.912
	PE	8.421e-13	5.511e-16	1.984e-13	1.124	0.9183
	MMSE	1.862e-26	2.051e-32	6.878e-28	0.021	0.016
2	RE	8.115e-12	8.115e-12	1.049e-12	9.013	8.5270
	PE	2.268e-12	7.771e-16	4.344e-13	1.9356	2.129
	MMSE	8.578e-26	2.054e-32	3.539e-27	0.086	0.0756
3	RE	1.961e-11	4.425e-16	3.270e-12	7.793	7.973
	PE	3.329e-12	1.221e-15	6.109e-13	2.1504	1.4071
	MMSE	1.848e-25	2.958e-32	2.207e-26	0.077	0.090
4	RE	1.961e-11	<b>8.881e-16</b>	1.442e-12	1.877	5.846
	PE	3.455e-12	<b>8.881e-16</b>	1.442e-12	0.721	1.612
	MMSE	4.016e-25	<b>2.054e-32</b>	6.031e-26	0.008	0.043
5	RE	9.9128	4.035e-15	9.023e-12	3.902	6.342
	PE	3.41e-12	9.92e-16	2.224e-12	0.790	1.769
	MMSE	4.142e-25	2.052e-32	8.265e-26	0.018	0.052

sampling and quantization errors, bumps are used for checking robustness against transient changes, heavysine test signal is used for testing the robustness against phase variations and Chirp signal is used for testing the frequency variations. The data for test signals is obtained from Gaussian Random generator with mean value as 0 and standard deviation of 1. The wavelet test signals[26] are the benchmark signals that characterize the proposed method. From Table 3, it is clear that MMSE for chirp signal is very less compared to other test signals. The maximum Peak Error between the source and the reconstructed profile of the chirp signal is minimum when compared to other test signals. This shows that the proposed algorithm can better handle the frequency variations without loss of information in the reconstructed profiles.

### 3.4. Effect of wavelet, dictionary leaning, and IFE parameters on doppler shift

The optimal combination of Wavelet parameters like the number of decomposition, the type of Wavelet(Daubechies(db4), Haar, Symlet(sym4), Coiflets(coif4), Fejer-Korovkin(fk4)), the Dictionary Learning parameters like patch size, and the IFE parameters like window size are chosen using the performance indicators mentioned in (11), (12), and (13). The number of levels of Decomposition are chosen based on the Wavelet type that has the lowest value of RE. From the Table 4, the PE and MMSE for 'Haar' Wavelet with 3 levels of levels of decomposition are less compared to 4 levels of decomposition, but their RE follow the opposite trend.

#### 3.4.1. Type of wavelet

The Fig. 7 represents the decomposition of a single temporal profile into 5 levels of decomposition having time period of 8 min, 16 min, 32 min, 64 min, and 128 min respectively. For all the levels of decomposition, the coif4 and fk4 wavelets produce the waves ahead of with 'db4', 'Haar', and 'sym4' Wavelets. From Table 4 and Fig. 7, a combination of 'Haar' wavelet with 5 levels of decomposition is considered in the present work based on low value of RE.

#### 3.4.2. Decomposition levels

The number of levels of decomposition have impact only on the amplitude of the Doppler component due to background wind. The

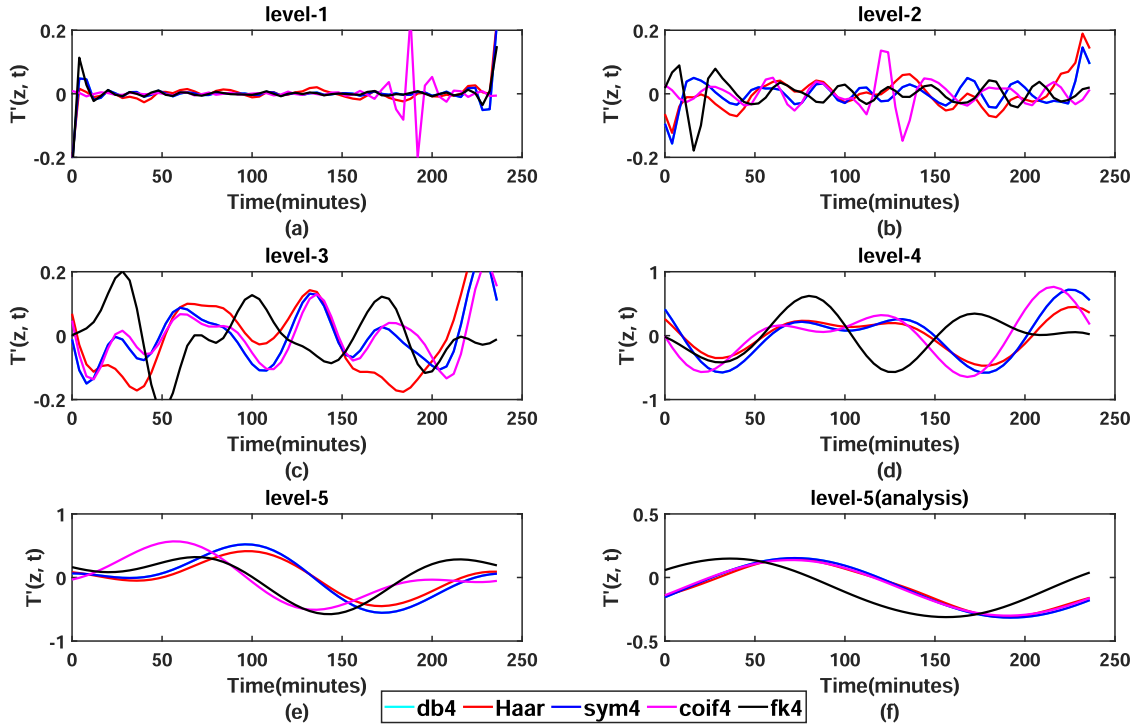


**Fig. 7.** Comparison of Wavelet decomposition of a single temporal profile using db4, Haar, sym4, coif4 and Fejer-Korovkin(fk4) Wavelets through Multi Resolution Analysis with detail coefficients with time period of (a) 8 min, (b) 16 min, (c) 32 min, (d) 64 min, (e) 128 min and (f) analysis coefficients of level 5. The decomposition using 'db4' exactly coincide the decomposition obtained using 'Haar' Wavelet and is not seen due to a difference in order of  $10e-25$ .

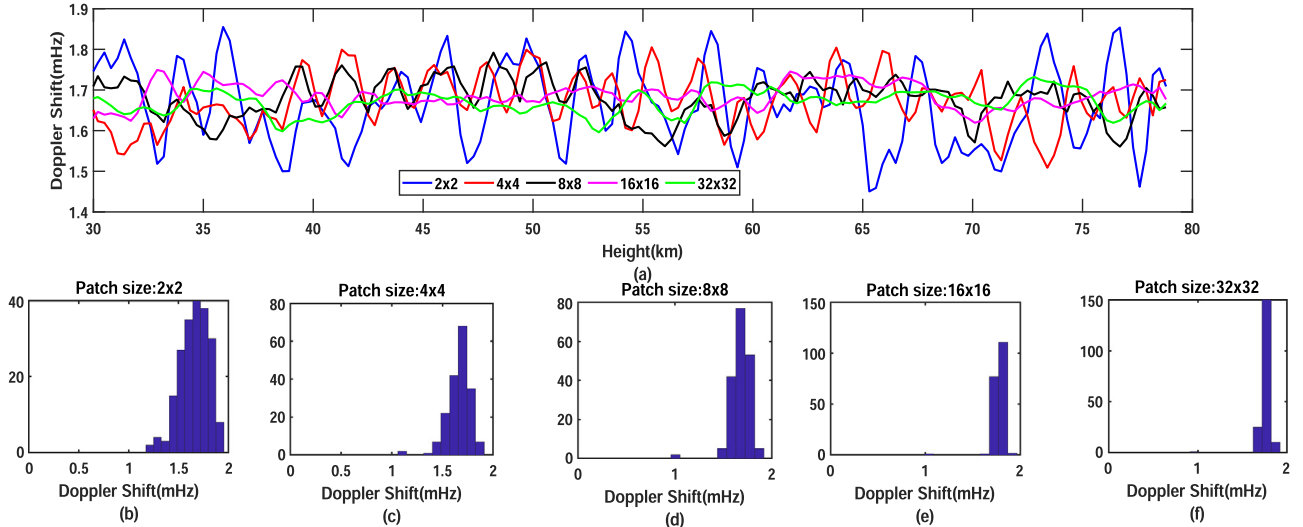


**Fig. 8.** Effect of patch size on the Doppler shift. (a) Variation of Doppler shift profile with patch size. (b), (d), (e), (f) represent the efficiency of patch size in preserving the small changes in Doppler Shift.

more the number of levels of decomposition, the better the representation subject to RE. So for the present temporal profiles, a maximum of 5 levels of decomposition are used. The number of levels of decomposition are limited by temporal resolution of measured data profiles.

### 3.4.3. Patch size

To assess the performance of choosing different patch size while applying Dictionary Learning, the Doppler Shift profiles are retrieved with patch size of  $2 \times 2$ ,  $4 \times 4$ ,  $8 \times 8$ ,  $16 \times 16$ , and  $32 \times 32$  are shown in Fig. 8(a). The patch size of  $2 \times 2$  give more informa-

tion about variations in Doppler shift than the other patch sizes, as seen from Fig. 8(a), and used in the present work. With increase in the size of patch, the Doppler Shift profile is more biased towards the maximum value. A larger patch size results in loss of information about lower values of Doppler Shift and can be observed from histograms in Fig. 8(b-f).

### 3.4.4. Window size

The window size used in the transform technique in the present work is of 20.6 mHz and don't have any effect on the Doppler shift values.

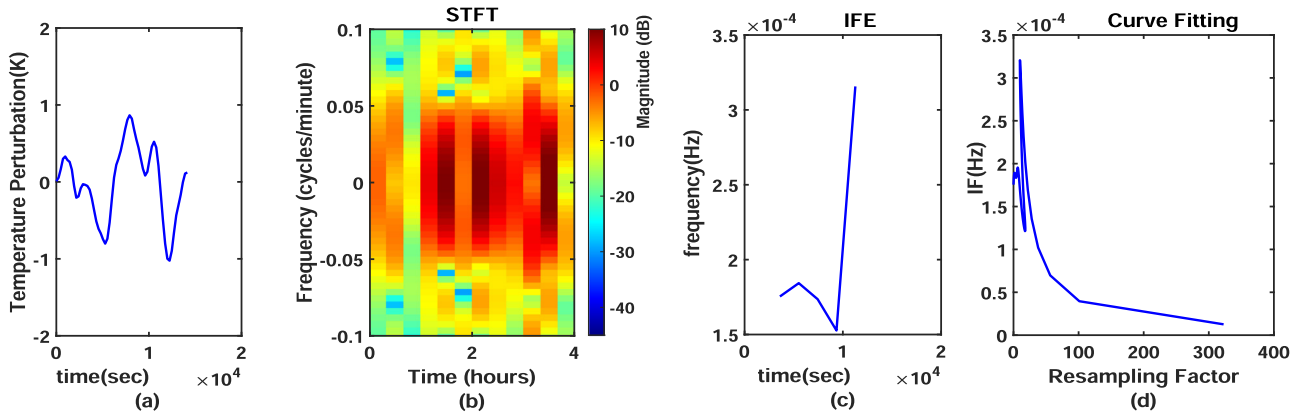


**Fig. 9.** Intermediate stages of the IFE method. (a) Temporal perturbation profile, (b) short Time Fourier Transform of temporal perturbation profile (c) Estimation of Instantaneous Frequency(IF), (d) Estimation of resampling Factor for correction of background wind effect.

### 3.5. Procedure for applying MRDL and IFE

To demonstrate the potential of the proposed method, we start by looking at the RE. The representation of data using a trained Dictionary is obtained by implementing the following steps.

1. Implement MRA on the training data.
2. Apply the iterative shrinkage algorithm to all levels of decomposition for obtaining the sparse representation of the transformed data using (5).
3. The resultant, after learning at each level is a sparse matrix and a Dictionary matrix.
4. Apply the IFE technique to sparse matrix at each level of decomposition for reducing the effect of background wind using (6) and (7).
5. Reconstruct the perturbation profiles( $\hat{\mathbf{Y}}$ ) using (8).

The Mutual Coherence( $\mu$ ) is used to quantify the Dictionary. A value of Mutual Coherence closer to zero indicates that the atoms in Dictionary are highly uncorrelated and ensures the Dictionary can represent the test data. The Mutual coherence is always between [0,1] and is 0.0485 for the present learned Dictionary. In the present work, the hyper-parameters in the Dictionary Learning process are obtained by the random search method and learning rate of 0.01 is used for Dictionary training.

### 3.6. Applying the IFE for retrieving Doppler shift

For explanation, the application of IFE is discussed for a single temporal profile at a particular altitude. The temporal profile is considered at an altitude of 45 km. The procedure is repeated for all the temporal profiles for reducing the effect of the background wind.

The selected temporal profile is shown in Fig. 9(a), is represented in both the Time and the Frequency domain using STFT, as shown in Fig. 9(b). A sampling frequency( $f_0$ ) of 4.16 mHz, and a window width of is 20.64 mHz is used. The Instantaneous Frequency(IF) curve shown in Fig. 9(c), for each sampling interval is calculated by using (12). The IF varies between 0.169 mHz to 0.363 mHz. The Doppler shift is reduced by resampling the timing intervals of measured temporal perturbation by the resampling factor. The resampling factor is obtained by non-linear least-squares fitting of the IF vector and sampling frequency vector with 95% of confidence that the effect of horizontal background wind get removed is shown in, Fig. 9(d). The model parameters for the fitting are given below:

$$\hat{\mathbf{f}}_{IF} = \mathbf{a} * (\mathbf{f}_{IF} - \mathbf{b})^{\hat{n}} \quad (14)$$

where  $\mathbf{a} = 1.657\text{e-}07$  lies in the interval  $(-9.578\text{e-}08, 4.272\text{e-}07)$ ,  $\mathbf{b} = 6478$  lies in the interval  $(1938, 1.102\text{e+}04)$  and  $\hat{n} = 1$ . Division of  $\hat{\mathbf{f}}_{IF}$  by  $\mathbf{f}_s$  will provide the resampling factor. The goodness of fitting is measured using Sum of Squares due to Error(SSE), R-Square, Adjusted R-square, and Root Mean Square Error(RMSE). The response and predicted response refers to the actual value of the Doppler shift and the Doppler shift obtained through IFE. For the present fitting technique used in this work, SSE is  $7.45\text{e-}7$ , R-square is 0.833, Adjustable R-Square value is 0.732 and RMSE is  $4.98\text{e-}4$ .

### 3.7. Comparison to other instruments

The retrieved Doppler shift profiles are validated using ground based instruments(GPS Radiosonde, Meteor Radar), and Horizontal Wind Model(HWM). The Doppler shift profiles obtained by using proposed method are compared with Doppler shift profiles calculated by using (A. 3) from wind velocity data acquired through GPS Radiosonde at Gadanki( $13.45^\circ\text{N}$ ,  $79.16^\circ\text{E}$ ) and Meteor Radar at Sri Venkateswara University, Tirupati( $13.63^\circ\text{N}$ ,  $79.40^\circ\text{E}$ ). The Rayleigh Lidar system is generally operated during nighttime between 19:00 h to 05:00 h Local Time(LT) subject to clear sky conditions.

NARL launches GPS Radiosonde (RD-11G, Meisei make) every day around 17 h 30 min Local Time (12 UTC). The GPS Radiosonde provides profiles of Pressure, Temperature, Relative humidity, Wind Speed, and Wind Direction up to the balloon burst altitude typically 30 km to 35 km. The maximum height reached by Radiosonde is 33 km on 21 April 2014.

The Meteor Radar(MR) operates at 35.25 MHz, was installed at Sri Venkateswara University (SVU), Tirupati, India, for the observation of horizontal winds in the Mesosphere and Lower Thermosphere (MLT). The MR operates continuously in all days except a few days that are used for maintenance of MR. The MR is located 30 km away from the Gadanki, which gives information about winds in the region between 70 km and 110 km with a spatial resolution of 2 km.

The Horizontal Wind Model(HWM) [27] is an empirical horizontal neutral wind model. The model represent the changes in the middle and upper atmosphere winds based on insitu solar heating, influence of the earths rotation, tilt, and orbit around the sun. The HWM provides zonal and meridional winds for specified latitude, longitude, and time with a vertical altitude resolution of 1 km. The root mean square differences of the data and model values are 15 m/s in the mesosphere and 10 m/s in the stratosphere for zonal winds, and 10 m/s and 5 m/s respectively for meridional winds. The Doppler shift profile in the height region between 25 km to 35 km and 72 km to 80 km is obtained by substituting



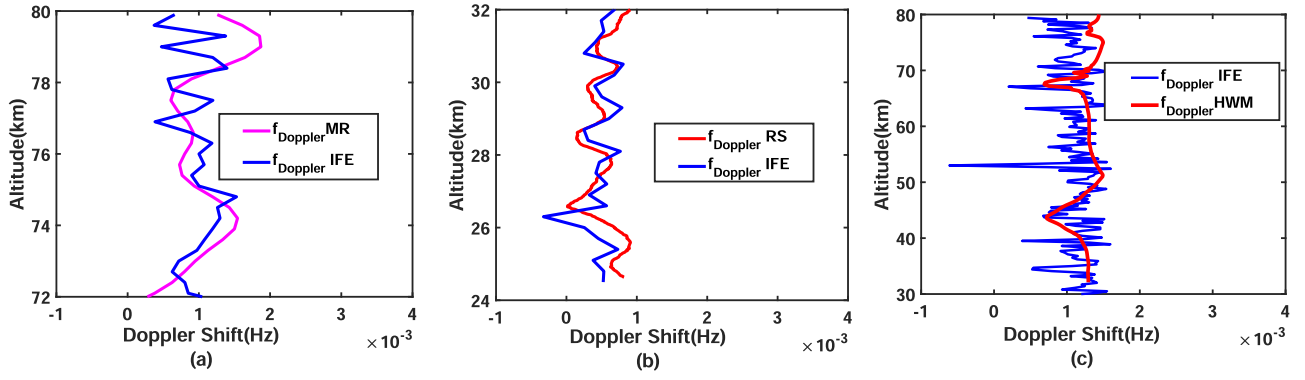


**Fig. 10.** Comparison of Doppler Shift profile. (a) Comparison of Doppler Shift profile retrieved with IFE and Meteor Radar in the 72 km to 80 km vertical height, (b) Comparison of Doppler Shift profile retrieved with IFE and GPS Radiosonde in the vertical height of 25 km to 35 km, (c) Comparison of Doppler Shift profile obtained through IFE and Horizontal Wind Model in the height region between 30 km to 80 km region.

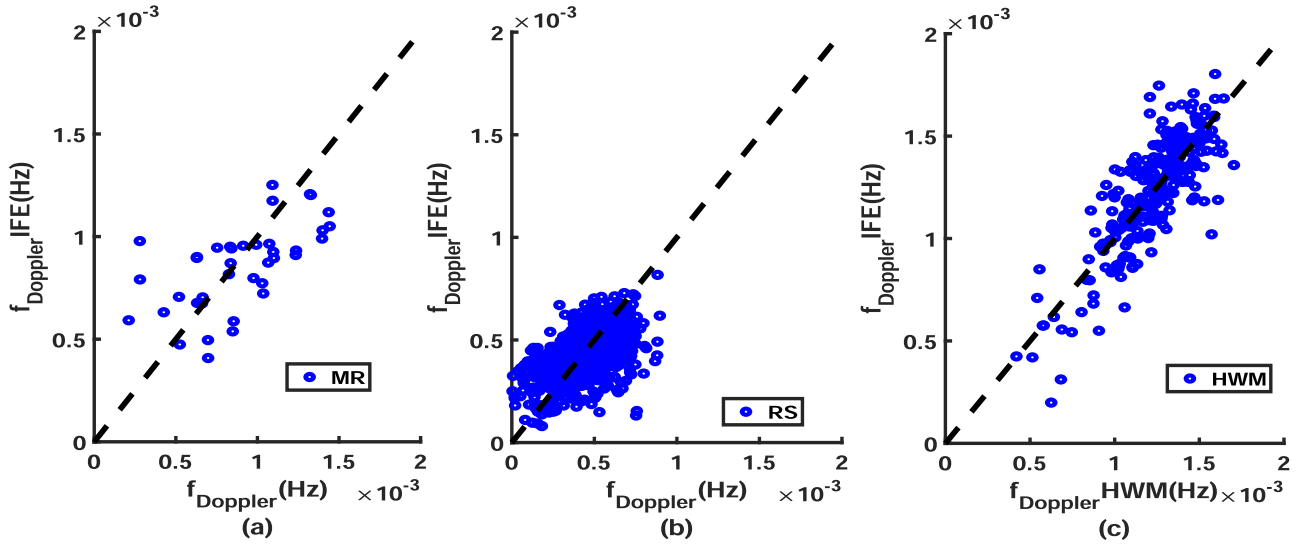


**Fig. 11.** Comparison of retrieved Doppler shift with Doppler shift retrieved from (a) Meteor Radar (MR) with a spatial resolution of 2 km in altitude region between 70 km to 80 km, (b) Radiosonde (RS), with a spatial resolution of 0.3 km in altitude region between 25 km to 35 km and (c) Horizontal Wind Model (HWM) with a spatial resolution of 1 km for the data collected in altitude region between 30 km to 80 km on 7 April 2014, 21 April 2014, 9 January 2015, and 11 August 2016. The data of all the instruments is available on these days.

the zonal wind data, wind direction information, and horizontal wavelength of 20 km in (A. 3). The angle between the horizontal wavenumber and the zonal wind is calculated by using the dot product.

All three systems are operated on 21 April 2014 and their data is considered for the present work for comparison. For both Radiosonde and MR, the Doppler shift is calculated from the dot product of the wavenumber vector and velocity vector. The comparison of Doppler shift profiles obtained through IFE and MR are shown in Fig. 10(a). The Doppler shift profile obtained through IFE has large fluctuations when compared to MR. A poor value of SNR of Lidar at higher altitudes is the reason for large fluctuations in the height region between 72 km to 80 km. A percentage difference of 0 to 3 in Doppler shift is observed in the altitude between 70 km to 76 km. Above the 78 km where the SNR is low, the Doppler shift retrieved cannot be trusted. While at the lower heights between 24 km to 32 km, the Doppler profile retrieved with GPS Radiosonde has a good correlation with the Doppler shift profile obtained through IFE as shown in Fig. 10(b). The percentage difference in Doppler shift using Radiosonde and Instantaneous Frequency Estimation varies from 0 to 0.2. The Doppler shift varies from 0 mHz to 1.7 mHz in the altitude between 30 km to 80 km. The Rayleigh scattering is dominant in the altitude region start-

ing altitude between 30 km to 80 km. Comparison of Doppler shift retrieved from Horizontal Wind Model [27] and Instantaneous Frequency Estimation is given in Fig. 10(c). The cross-correlation coefficient value of IFE with MR and RS are 0.72 and 0.85 as observed from Fig. 11(a), and (b) respectively. The retrieved Doppler shift profiles are compared with Doppler shift retrieved from wind velocities obtained from Horizontal Wind Model (HWM) as shown in Fig. 11(c). From Fig. 11(c) the Doppler shift retrieved through IFE is more than the Doppler Shift obtained through HWM. The cross-correlation coefficient between IFE and HWM is 0.7.

### 3.8. Ensuring the removal of background source

The criteria for ensuring the removal of background wind in remnant temperature perturbations ( $T'(z, t)_{\text{remnant}}$ ) is reported in [28] and defined as “the background remnants are smaller than the errors introduced by the instrument and the algorithm used for the temperature retrieval” and represented mathematically in (15). In the observation of perturbations like Gravity Waves, the uncertainty is more correlated to the precision than the instrument accuracy.

$$\langle T'(z, t)_{\text{remnant}} \rangle \ll \left[ \Delta T_S + \Delta T_R \right]_{\text{Precision}} + \left[ \Delta T_M \right]_{\text{Accuracy}} \quad (15)$$

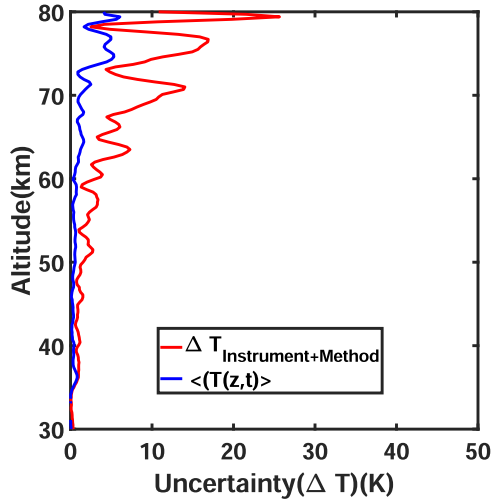


**Fig. 12.** Comparison of mean of remnant temperature perturbations with the uncertainty budget having a spatial resolution of 300 m and time integration for 4 h for the data collected on 21 April 2014.

**Table 5**

The Uncertainty Budget for NARL Rayleigh Lidar System. (.)/(.) indicates the uncertainty in high intensity and low intensity channels.

Source	80 km	70 km	50 km	30 km
$N_D$	6K/(.)	5K/(.)	1K/4K	(.)/0.08K
$N_B$	0.5K/(.)	0.3K/(.)	0.3K/(0.8)	(.)/0.02K
Seed temperature	4K	2K	0.5K	-
Gravity(g)	0.1K	0.1K	0.1K	0.1K
$M_{dryair}$	1K	0.05K	0.05K	0.05K
Method	15K	8K	3K	0.08K
Total Uncertainty	27K/40K	16K/(.)	4.8K/8.45 K	0.08K/0.33K

$N_D$  indicates the Detection Noise and  $N_B$  indicates the background noise.

where  $T'(z, t)_{remnant}$  represent the reconstructed temperature perturbations after removing the effect of background wind,  $\Delta T_S$  indicates the systematic uncertainty,  $\Delta T_R$  indicates the random uncertainty,  $\Delta T_M$  is the uncertainty introduced by the  $KKTl_2$  algorithm [17] used for atmospheric temperature retrieval.

The mean of the temperature perturbations after removing the effect of background wind, and the uncertainty budget of the instrument and the algorithm used for temperature retrieval are shown in Fig. 12. The uncertainty in temperature profiles due to different sources is calculated using the procedure followed in [29]. The uncertainty in temperature profiles due to different sources for the high intensity and the low-intensity channels are mentioned separately in Table 5. An empty brace indicates that there is no contribution of the source of that channel to the uncertainty at a specific altitude. A maximum value of uncertainty of 20K to 40K is observed at 80 km. The contribution to uncertainty from acceleration due to gravity and the molecular mass of dry air is negligible.

A comparison of RE using MRDL and Wavelet Packet Decomposition based on the % of coefficients used for reconstruction is given in Fig. 13. For a good method, the RE is less for a fixed percentage of the coefficients used for reconstruction. The difference in the RE obtained using WPD and MRDL is of 12% on using 15% wavelet coefficients, the difference in RE reduces to 5% on using 85% wavelets coefficients for reconstruction and on using 100% wavelet coefficients used for reconstruction, WPD has the RE of 5% and the RE for MRDL limits to 0.

### 3.9. Seasonal variations in Doppler shift

The distribution of Doppler Shift for the data available in each season of 2014 are shown in Fig. 14(a)–(c) respectively. The statis-

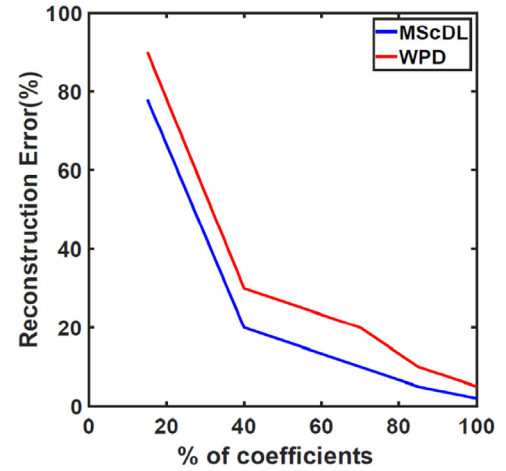


**Fig. 13.** Comparison of RE in using Multi-Resolution Dictionary Learning(MRDL) and Wavelet Packet Decomposition(WPD).

**Table 6**

Seasonal variations of distribution function of the Doppler shift in the year 2014.

Season	Winter	Summer	Southwest Monsoon
No. of. Days	11	7	9
Vertical Wavelength(km)	2, 3, 5 to 7	8 to 12	7 to 12
	8, 10 to 15	13 to 15	7 to 12
$f_{dmax}$ (mHz)	1.7	1.7	1.7
$f_{dmin}$ (mHz)	0.376	0.383	0.322
$\mu$ (mHz)	1	1.04	1.01
$\sigma$ (mHz)	0.24	0.226	0.23
Skewness	0.186	-0.102	-0.08
Kurtosis	-0.39	-0.14	-0.289

$\mu$  and  $\sigma$  indicate the mean and Standard deviation of distribution.

tical studies are conducted on Doppler shift profiles retrieved in all the seasons for the year 2014. The normal distribution is fitted to the histogram to infer the Doppler shift distribution. The Skewness and Kurtosis with 99.9 confidence interval for Doppler shift are given in Table 6. The seasons at the observational site are divided into winter (December, January, and February), summer(March, April, and May), North-East monsoon(June, July, and August),and South-West monsoon(September, October, and November). Due to non-availability of data in the North East Monsoon season, variations in this season are not indicated. In summer season, the intrinsic frequency is perfectly correlated to altitude than the other seasons. The statistics in Table 6 reveal that the Doppler shift clearly deviate from the normal distributions. The following inferences are made from the Table 6. The negative values of Skewness and Kurtosis indicates that most of the information about Doppler shift is obtained from the negative tail of the distribution function.

1. The minimum value of Doppler shift occur in the Southwest Monsoon season and the maximum value of Doppler shift reaches to 1.7 mHz in all seasons.
2. The standard deviation of Doppler shift is more in winter season and a minimum value of standard deviation is observed in summer season.
3. The distribution curves of Doppler shift in all the seasons are moderately skewed. In Southwest Monsoon season, a minimum value of skewness indicates that the Doppler Shift profiles follows Normal distribution functions. The distribution function of Doppler shift profiles in Winter season depart from Normal distribution due to large variations in the horizontal wind.

The present findings about the Doppler shift can be viewed as support to incorporate the effects of background wind in the

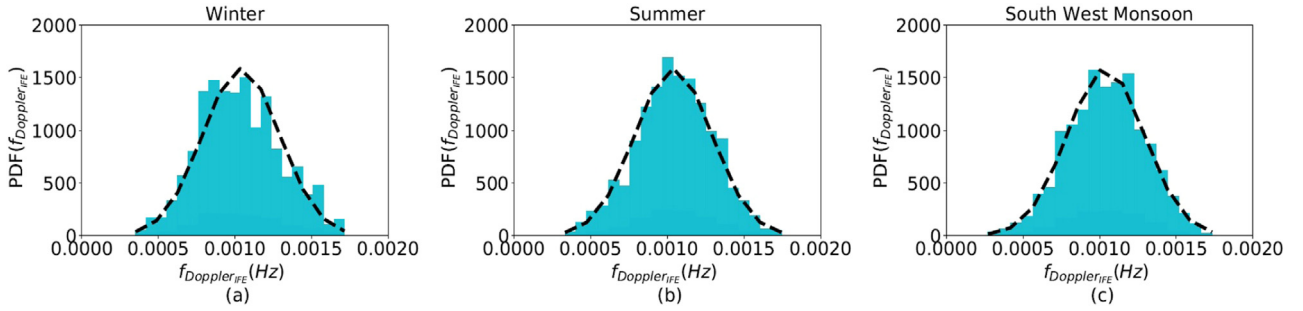


**Fig. 14.** Seasonal variations in the distribution of Doppler shift for the year 2014. (a), (b), and (c) indicates the distribution of Doppler Shift in Winter, Summer, and Southwest Monsoon Seasons respectively.

Parametrization of the Gravity Waves. The findings of the present study (like seasonal variations in mean and kurtosis of Doppler frequency distribution) about the effect of background wind on seasonal variations of Doppler Shift agree with the arguments reported in [20].

#### 4. Conclusion

In this work, we presented a methodology for reducing the effect of other background sources in the measured data profiles using Multi-Resolution Dictionary Learning and Instantaneous Frequency Estimation. The data is decomposed to different temporal resolutions using Wavelet decomposition. The Dictionaries are trained for all the decomposition levels in the analysis domain of the Wavelet transform. The learned effective Dictionary outperforms both fixed analytic transforms (DWT, DCT) and single resolution learned Dictionaries. The proposed algorithm is more suitable to the case when measured data is effected by background sources in the amplitude and in the frequency domain. The proposed algorithm is applied to the case of reducing the effect of background wind in Gravity Wave Signatures.

The effect of selecting the Wavelet type, number of levels of decomposition, patch size and Window size on Doppler shift are discussed. Harr Wavelet with 4 levels of decomposition and patch size of  $2 \times 2$  are chosen as optimal values for the Multi-Resolution Dictionary Learning Technique proposed.

The obtained Doppler shift profiles are compared to the Doppler frequency shift at respective altitudes, calculated by using wavenumber, zonal wind, and wind direction obtained from GPS Radiosonde and Meteor Radar from RS, MR, and HWM. After reconstruction, the profiles are checked for any background wind remnants in the temperature perturbations. The seasonal variations of Doppler shift are studied and observed that in Winter season the distribution of Doppler shift values depart significantly from Normal distribution when compared to other seasons.

#### Funding

This research work was funded by the National Atmospheric Research Laboratory, Department of Space, Gadanki, Andhra Pradesh, India.

#### Data availability

The data used in the present work is available at <https://www.narl.gov.in>. The data of the Horizontal Wind Model is available at <https://www.alpendac.eu>

#### Declaration of Competing Interest

The authors declare that they have no known competing financial interests or personal relationships that could have appeared to influence the work reported in this paper.

#### CRediT authorship contribution statement

**Varanasi Satya Sreekanth:** Writing – review & editing, Conceptualization, Methodology, Software, Visualization, Formal analysis. **Karnam Raghunath:** Writing – review & editing, Conceptualization, Supervision. **Deepak Mishra:** Writing – review & editing, Conceptualization, Supervision.

#### Data Availability

Data will be made available on request.

#### Acknowledgment

We are also thankful to Dr. M. Venkatratnam, ARTG, NARL and Prof. Dr. S. Vijaya Bhaskara Rao, Department of Physics, Sri Venkateswara University, Tirupati, for helping us in the extraction of Gravitywave Parameters and providing us the GPS Radiosonde and Meteor Radar data.

#### Appendix A. Atmospheric gravity waves

The Gravity Waves generated in the Troposphere ( $\leq 15$  km) reach the Upper Mesosphere (90 km) as an almost monochromatic wave packet with a horizontal wavelength between a few kilometers and more than 100 km depending on the forcing and the background conditions. The vertical displacement field ( $\zeta$ ) for a travelling wave due to perturbation is given by

$$\zeta(x, z, t) = A_{\zeta} \cos(k\mathbf{a}_x + m\mathbf{a}_z - \hat{\omega}t) \quad (\text{A.1})$$

where  $k$  and  $m$  are the real-valued horizontal and vertical wavenumbers. The  $x$ -axis represents the time frame of observation, and the  $z$ -axis represent the vertical height of the atmosphere. The wave frequency  $\hat{\omega} = \frac{2\pi}{T}$  ( $T$  is wave period) is derived from the dispersion relation for internal waves as given by

$$\hat{\omega} = N^2 \frac{k^2}{k^2 + m^2} = N \cos(\phi) \quad (\text{A.2})$$

where  $N$  is the Buoyancy frequency at the stable environment,  $\phi$  is angle between the wavenumber vector  $\mathbf{K}$  and the background horizontal wind ( $\bar{U}$ ). The sign combination of wavenumber components and sign of  $\phi$  reveal information about the upward or downward, and the leftward or rightward propagating waves. The background wind ( $\bar{U}$ ) makes the observed frequency as

the Quasi-Doppler-shifted( $f_d = (\tilde{\mathbf{K}} \cdot \tilde{\mathbf{U}}) / (2\pi)$ ) version of the intrinsic frequency as given in (A.3)

$$f_{obs} = f_{intrinsic} + \frac{|\tilde{\mathbf{K}}| |\tilde{\mathbf{U}}| \cos(\theta_r)}{2\pi} \quad (\text{A.3})$$

where  $\tilde{\mathbf{K}} = \mathbf{k}\mathbf{a}_x + \mathbf{m}\mathbf{a}_z$ ,  $\tilde{\mathbf{U}} = \mathbf{u}\mathbf{a}_x + \mathbf{v}\mathbf{a}_z$ ,  $\theta_r$  is the angle between the zonal wind component ( $u$ ) and the horizontal wavenumber( $k$ ), and  $v$  is the meridional wind component of horizontal wind.

## References

- [1] F. Chane-Ming, F. Molinaro, J. Leveau, Wavelet techniques applied to lidar temperature profiles in the middle atmosphere to study gravity waves, in: IGARSS'97. 1997 IEEE International Geoscience and Remote Sensing Symposium Proceedings. Remote Sensing-A Scientific Vision for Sustainable Development, vol. 1, IEEE, 1997, pp. 581–583.
- [2] F. Chane-Ming, F. Molinaro, J. Leveau, P. Keckhut, A. Hauchecorne, Analysis of gravity waves in the tropical middle atmosphere over la reunion island (21 s, 55 e) with lidar using wavelet techniques, in: Annales Geophysicae, vol. 18, Copernicus GmbH, 2000, pp. 485–498.
- [3] A. Yadav, A. Aryasomayajula, R. AhmedAnsari, Multiresolution analysis based sparse dictionary learning for remotely sensed image retrieval, in: 2019 Women Institute of Technology Conference on Electrical and Computer Engineering (WITCON ECE), IEEE, 2019, pp. 76–80.
- [4] J. Medel, A. Savakis, B. Ghorani, A novel time-frequency feature extraction algorithm based on dictionary learning, in: 2016 IEEE International Conference on Acoustics, Speech and Signal Processing (ICASSP), IEEE, 2016, pp. 4895–4899.
- [5] R. Rubinstein, A.M. Bruckstein, M. Elad, Dictionaries for sparse representation modeling, Proc. IEEE 98 (6) (2010) 1045–1057.
- [6] M. Aharon, M. Elad, A. Bruckstein, K-SVD: an algorithm for designing overcomplete dictionaries for sparse representation, IEEE Trans. Signal Process. 54 (11) (2006) 4311–4322.
- [7] E.C. Marques, N. Maciel, L. Naviner, H. Cai, J. Yang, A review of sparse recovery algorithms, IEEE Access 7 (2018) 1300–1322.
- [8] M. Zibulevsky, M. Elad, L1-L2 optimization in signal and image processing, IEEE Signal Process. Mag. 27 (3) (2010) 76–88.
- [9] R. Rubinstein, M. Zibulevsky, M. Elad, Double sparsity: learning sparse dictionaries for sparse signal approximation, IEEE Trans. Signal Process. 58 (3) (2009) 1553–1564.
- [10] B. Ophir, M. Lustig, M. Elad, Multi-scale dictionary learning using wavelets, IEEE J. Sel. Top Signal Process. 5 (5) (2011) 1014–1024.
- [11] N.A. Khan, B. Boashash, Instantaneous frequency estimation of multicomponent nonstationary signals using multiview time-frequency distributions based on the adaptive fractional spectrogram, IEEE Signal Process. Lett. 20 (2) (2012) 157–160.
- [12] A. Neumaier, Solving ill-conditioned and singular linear systems: a tutorial on regularization, SIAM Rev. 40 (3) (1998) 636–666, doi:10.1137/S0036144597321909.
- [13] M.H. Alkinani, M.R. El-Sakka, Patch-based models and algorithms for image denoising: a comparative review between patch-based images denoising methods for additive noise reduction, EURASIP J. Image Video Process. 2017 (1) (2017) 1–27.
- [14] E. Treister, I. Yavneh, A multilevel iterated-shrinkage approach to  $l_1$  penalized least-squares minimization, IEEE Trans. Signal Process. 60 (12) (2012) 6319–6329.
- [15] C.D. Sigg, T. Dikk, J.M. Buhmann, Learning dictionaries with bounded self-coherence, IEEE Signal Process. Lett. 19 (12) (2012) 861–864.
- [16] Y. Abdouh, G. Pojani, G.E. Corazza, Adaptive instantaneous frequency estimation of multicomponent signals based on linear time-frequency transforms, IEEE Trans. Signal Process. 67 (12) (2019) 3100–3112.
- [17] V.S. Sreekanth, K. Raghunath, D. Mishra, Dictionary learning technique and penalized maximum likelihood for extending measurement range of a rayleigh lidar, J. Appl. Remote Sens. 14 (3) (2020) 034529.
- [18] A. Dörnbrack, S. Gisinger, B. Kaifler, On the interpretation of gravity wave measurements by ground-based lidars, Atmosphere 8 (3) (2017) 49.
- [19] V. Siva Kumar, P.B. Rao, M. Krishnaiah, Lidar measurements of stratosphere-mesosphere thermal structure at a low latitude: comparison with satellite data and models, J. Geophys. Res. Atmos. 108 (D11) (2003).
- [20] S.D. Eckermann, Effect of background winds on vertical wavenumber spectra of atmospheric gravity waves, J. Geophys. Res. Atmos. 100 (D7) (1995) 14097–14112.
- [21] M.V. Ratnam, N. Pravallika, S.R. Babu, G. Basha, M. Pramitha, B.K. Murthy, Assessment of GPS radiosonde descent data, Atmos. Meas. Tech. 7 (2014) 1011–1025.
- [22] S.V.B. Rao, S. Eswaraiyah, M. Venkat Ratnam, E. Kosalendra, K. Kishore Kumar, S. Sathish Kumar, P. Patil, S. Gurubaran, Advanced meteor radar installed at Tirupati: system details and comparison with different radars, J. Geophys. Res. Atmos. 119 (21) (2014) 11–893.
- [23] D.C. Fritts, T. VanZandt, Effects of doppler shifting on the frequency spectra of atmospheric gravity waves, J. Geophys. Res. Atmos. 92 (D8) (1987) 9723–9732.
- [24] B. Ehard, B. Kaifler, N. Kaifler, M. Rapp, Evaluation of methods for gravity wave extraction from middle-atmospheric lidar temperature measurements, Atmos. Meas. Tech. 8 (11) (2015) 4645–4655.
- [25] V.N. Gubenko, A.G. Pavelyev, V.E. Andreev, Determination of the intrinsic frequency and other wave parameters from a single vertical temperature or density profile measurement, J. Geophys. Res. Atmos. 113 (D8) (2008).
- [26] D.L. Donoho, J.M. Johnstone, Ideal spatial adaptation by wavelet shrinkage, Biometrika 81 (3) (1994) 425–455.
- [27] D. Drob, J. Emmert, G. Crowley, J. Picone, G. Shepherd, W. Skinner, P. Hays, R. Niciejewski, M. Larsen, C. She, et al., An empirical model of the Earth's horizontal wind fields: HWM07, J. Geophys. Res. Space Phys. 113 (A12) (2008).
- [28] C. Strube, M. Ern, P. Preusse, M. Riese, Removing spurious inertial instability signals from gravity wave temperature perturbations using spectral filtering methods, Atmos. Meas. Tech. 13 (9) (2020) 4927–4945.
- [29] T. Leblanc, R.J. Sica, J.A. Van Gijzel, S. Godin-Beekmann, A. Haefele, T. Trickl, G. Payen, G. Liberti, Proposed standardized definitions for vertical resolution and uncertainty in the NDACC lidar ozone and temperature algorithms—Part 2: ozone dial uncertainty budget, Atmos. Meas. Tech. 9 (8) (2016) 4051–4078.